coastal regions. The simulated current, upon entering the subtropical Tethys Ocean, is driven back into the tropics and into the Pacific Ocean by strong northeasterly wind stress (see Fig. 1).

In the model, the mean depth of the TCC varies substantially, depending on the width of the channel in which it flows (Fig. 3). In the narrow Tethys Seaway, the TCC attained its maximum vertical extent of ~350 m, whereas in the broad Pacific basin, its vertical scale was less than 100 m (basin depths would therefore need to be of order 100 m for such a surface current to be seriously affected by bathymetry in a stratified ocean). The half-width of the TCC had its smallest value of 440 km in the Tethys Seaway and in the equatorial Pacific basin; its largest value of 1540 km was in the southern Tethys Ocean off the northern coast of South America. The predicted core velocity of the TCC ranged from ~43 cm/s in the Pacific to ~11 cm/s in the Tethys Seaway and Ocean. These parameters deliver a mass flux of 17 sverdrup in the Tethys Seaway, 29 sverdrup in the southern Tethys Ocean, and 13 sverdrup in the Pacific basin.

In such a relatively narrow channel as the Tethys Seaway, however, the surface currents might be strongly influenced by the seasonal south Eurasian monsoon, which in the present-day climate induces surface current reversals (from westward to eastward) off the northeast coast of Africa during the Northern Hemisphere summer. The simulated currents in the Tethys Seaway during June, July, and August (Fig. 4) do indeed display a reversed, eastward-flowing monsoon current near the surface. However, this current reversal occurs along the south Eurasian coast and does not countercheck the westward flow of the TCC. The TCC is 5 cm/s weaker than the annual mean during these monsoon months but remains a robust feature of the simulation. However, an increase of mixing and eddy kinetic energy through shear instability between the westward TCC and the eastward monsoon current should occur during the northern summer, as well as coastal upwelling along the south Eurasian coast, which may account for the geological evidence of coastal upwelling in the region (7).

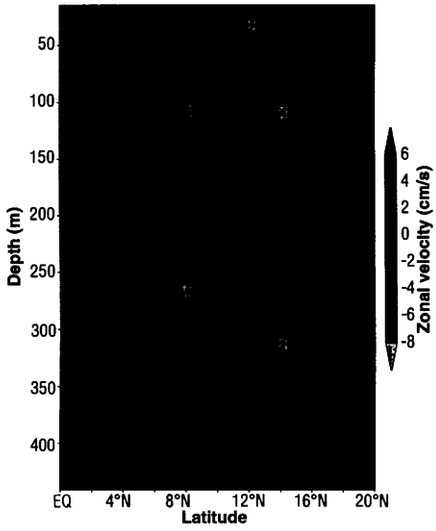

Fig. 4. Depth-latitude plots of the annual mean TCC at 50°E, as in Fig. 3A, but averaged over the Northern Hemisphere monsoon months of June, July, and August. The horizontal-velocity contour interval is 2 cm/s.

REFERENCES AND NOTES

1. A. Hallam, in *An Outline of Phanerozoic Biogeography*, A. Hallam, B. R. Rosen, T. C. Whitmore, Eds. (Oxford Univ. Press, Oxford, 1994), pp. 178–203.
2. F. Rogl and F. F. Steininger, in *Fossils and Climate*, P. Brenchley, Ed. (Wiley, New York, 1984), pp. 171–200.
3. B. P. Luyendyk, D. Forsyth, J. D. Phillips, *Geol. Soc. Am. Bull.* **83**, 2649 (1972); W. A. Gordon, *J. Geol.* **81**, 269 (1973).
4. B. U. Haq, in *Marine Geology and Oceanography of Arabian Sea and Coastal Pakistan*, B. U. Haq and J. D. Milliman, Eds. (Van Nostrand Reinhold, New York, 1984), pp. 201–231.
5. S. M. Stanley, *J. Paleontol.* **69**, 999 (1995); A. Hallam, in (2), pp. 107–125.
6. C. M. Janis, in (2), pp. 85–104.
7. K. B. Föllmi and M. Delamette, *Science* **251**, 94 (1991); E. J. Barron and W. H. Peterson, *ibid.*, p. 94.
8. E. J. Barron and W. H. Peterson, *ibid.* **244**, 684 (1989).
9. ———, *Paleoceanography* **5**, 319 (1990).
10. E. J. Barron and W. Washington, *J. Geophys. Res.* **89**, 1267 (1984).
11. C. T. Gordon and W. Stem, *Mon. Weather Rev.* **110**, 625 (1982).
12. R. C. Pacanowski, K. Dixon, A. Rosati, *GFDL Ocean Group Tech. Rep. 2* (Geophysical Fluid Dynamics Laboratory, Princeton, NJ, 1991).
13. S. Manabe and K. Bryan Jr., *J. Geophys. Res.* **90**, 11689 (1985).
14. S. Manabe and R. J. Stouffer, *Nature* **378**, 165 (1995).
15. P. A. Sandberg, *ibid.* **305**, 19 (1983).
16. A. M. Ziegler, C. R. Scotese, S. F. Barrett, in *Tidal Friction and Earth's Rotation II*, F. Brosche and J. Sundermann, Eds. (Springer-Verlag, Berlin, 1982).
17. E. J. Barron and W. Washington, *Geology* **10**, 633 (1982).

18. The author gratefully acknowledges the support of a University Corporation for Atmospheric Research Postdoctoral Fellowship in Ocean Modeling, as well as G. Philander for making this work possible.

30 October 1996; accepted 27 December 1996

Structure of DNA–Cationic Liposome Complexes: DNA Intercalation in Multilamellar Membranes in Distinct Interhelical Packing Regimes

Joachim O. Rädler,* Ilya Koltover, Tim Salditt, Cyrus R. Safinya†

Cationic liposomes complexed with DNA (CL-DNA) are promising synthetically based nonviral carriers of DNA vectors for gene therapy. The solution structure of CL-DNA complexes was probed on length scales from subnanometer to micrometer by synchrotron x-ray diffraction and optical microscopy. The addition of either linear λ-phage or plasmid DNA to CLs resulted in an unexpected topological transition from liposomes to optically birefringent liquid-crystalline condensed globules. X-ray diffraction of the globules revealed a novel multilamellar structure with alternating lipid bilayer and DNA monolayers. The λ-DNA chains form a one-dimensional lattice with distinct interhelical packing regimes. Remarkably, in the isoelectric point regime, the λ-DNA interaxial spacing expands between 24.5 and 57.1 angstroms upon lipid dilution and is indicative of a long-range electrostatic-induced repulsion that is possibly enhanced by chain undulations.

Somatic gene therapy depends on the successful transfer and expression of extracellular DNA to the nucleus of eucaryotic cells, with the aim of replacing a defective or adding a missing gene (1). Viral-based carriers of DNA are presently the most common method of gene delivery, but there has been a tremendous activity in developing synthetic nonviral vectors (2). In particular, cationic liposomes (CLs) (3), in which the overall positive charge of the cationic liposome-DNA (CL-DNA) complex enhances transfection by attaching to anionic animal cells, have shown gene expression in vivo in targeted organs (4), and human clinical protocols are ongoing (5). Cationic liposome transfer vectors exhibit low toxicity, nonimmunogenicity, and ease of production, but their mechanism of ac-

Materials Department, Physics Department, and Biochemistry and Molecular Biology Program, University of California, Santa Barbara, CA 93106, USA.

*Present address: Physikdepartment, Technische Universität München, Institut für Biophysik (E22), James Franck–Strasse, 85747 Garching, Germany.

†To whom correspondence should be addressed.

tion remains largely unknown; transfection efficiencies vary by up to a factor of 100 in different cell lines (*2*–*6*).

This unpredictability, which is ubiquitous in gene therapy (*7*) and in particular in synthetic systems, may be attributed to a lack of knowledge regarding the interactions between DNA and CLs and the resulting structures of CL-DNA complexes. DNA-membrane interactions might also provide clues for the relevant molecular forces in the packing of DNA in chromosomes and viral capsids. Studies show regular DNA condensed morphologies induced by multivalent cations (*8*) and liquid-crystalline (LC) phases at high concentrations of DNA both in vitro (*9*) and in vivo in bacteria (*10*). More broadly, the nature of structures and interactions between membranes and polymers, either adsorbed (*11*) or tethered to the membranes (*12*), is currently an active area of research.

Felgner *et al.* (*2*, *3*) originally proposed a "bead-on-string" structure of the CL-DNA complexes and pictured the DNA strand decorated with distinctly attached liposomes. Electron microscopy (EM) studies have reported on a variety of structures including stringlike structures and indications of fusion of liposomes in metal-shadowing EM (*13*), oligolamellar structures in cryo-transmission EM (*14*), and tubelike images possibly depicting lipid bilayer–covered DNA observed in freeze-fracture EM (*15*).

We have carried out a combined in situ optical microscopy and x-ray diffraction (XRD) study of CL-DNA complexes. On semi-macroscopic length scales, the addition of linear or circular plasmid DNA to binary mixtures of CLs induces a topological transition from liposomes into collapsed condensates in the form of optically birefringent LC globules with sizes on the order of 1 μm. The solution structure of the globules was revealed on the 1- to 100-nm length scale by high-resolution synchrotron XRD studies. Unexpectedly, the complexes consist of a higher ordered multilamellar structure with DNA sandwiched between cationic bilayers.

We have discovered distinct interhelical packing regimes for linear λ-phage DNA above, below, and at the isoelectric point of the complex by varying the concentrations of DNA and the lipid components comprising the complex. Remarkably, in the isoelectric regime of the CL-DNA complex, the DNA interaxial distance d_{DNA} increases from 24.5 to 57.1 Å as a function of lipid dilution and is quantitatively consistent with an expanding one-dimensional (1D) lattice of DNA chains. Thus, the DNA chains confined between bilayers form a novel 2D smectic phase.

DNA molecules can be readily labeled and imaged by fluorescence microscopy (*16*). Free λ-DNA in aqueous solution appears as a highly dynamic blob of ~1 μm in diameter, in agreement with a classical random coil configuration, whereas the contour length of λ-phage DNA is 16.5 μm. The CLs consisted of binary mixtures of lipids that contained either DOPC (dioleoyl-phosphatidylcholine) or DOPE (dioleoyl-phosphatidylethanolamine) as the neutral co-lipid and DOTAP (dioleoyl trimethylammonium propane) as the CL (*17*). The DOTAP/DOPC and DOTAP/DOPE CLs had a size distribution ranging between 0.02 to 0.1 μm in diameter, with a peak around 0.07 μm (*18*). We used highly purified linear λ-phage DNA (48,502 bp) in most of the experiments but some were carried out with *Escherichia coli* DNA and pBR322 plasmid DNA (4361 bp); the latter consisted of a mixture of nicked circular and supercoiled DNA (*19*). Condensation of CLs with λ-DNA was directly observed by using differential interference microscopy (DIC) and fluorescence microscopy (*20*).

We show in Fig. 1A a series of DIC images 30 min after preparation in CL-DNA mixtures as a function of the total lipid to λ-DNA weight ratio *L*/*D*, where *L* = DOTAP + DOPE denotes the weight of lipid and *D* is the weight of DNA. Similar images were observed with λ-DNA replaced by the pBR322 plasmid DNA or *E. coli* DNA, or DOPE replaced by DOPC. At low DNA concentrations (Fig. 1A, *L*/*D* = 50), in contrast to the pure liposome solution where no objects >0.2 μm were found, 1-μm globules were observed. The globules coexisted with excess liposomes. As more DNA was added, the globular condensates formed larger chainlike structures (Fig. 1A, *L*/*D* = 10). The Brownian motion of these globules suggests their linkage by an invisible thread. At *L*/*D* ≈ 5 the chainlike structures flocculated into large aggregates of distinct globules. For *L*/*D* <5, the complex size was smaller and stable in time again (Fig. 1A, *L*/*D* = 2), and coexisted with excess DNA. Fluorescence-labeled DNA and lipid could be detected on each globule, indicating that the globules are DNA-lipid condensates (*21*). Polarized microscopy also showed that the distinct globules were birefringent, indicative of their LC nature.

The size dependence of the complexes as a function of *L*/*D* (Fig. 1B) was independently measured by dynamic light scattering (*18*). The large error bars represent the broad polydispersity of the system. The size dependence of the aggregates can be understood in terms of a charge-stabilized colloidal suspension. The charge of the complexes was measured by their electrophoretic mobility in an external electric field (*22*). For *L*/*D* >5 (Fig. 1A; *L*/*D* of 50 or 10) the complexes are positively charged, while for *L*/*D* <5 (Fig. 1A; *L*/*D* of 2) the complexes are negatively charged. The charge reversal is in good agreement with the stoichiometrically expected charge balance of the components DOTAP and DNA at *L*/*D* ≈ 4.4, where *L* = DOTAP + DOPE in equal weights. Thus, the positively and negatively charged globules at *L*/*D*s of 50 and 2, respectively, repelled each other and remained separate while, as *L*/*D* approached 5, the nearly neutral complexes collided and tended to stick due to van der Waals attraction. Remarkably, the size of the globules appears to be only weakly dependent on the length of the DNA in similar experiments carried out with *E. coli* DNA or pBR322 plasmid (4361 bp) (*22*).

The XRD experiments (*23*) revealed unexpected structures for mixtures of CLs and DNA. Small-angle x-ray scattering (SAXS) data of dilute (Φ_w = the volume fraction of water = 98.6 ± 0.3%) DOPC/DOTAP (1:1)–λ-DNA mixtures as a function of *L*/*D* (*L* = DOPC + DOTAP) (Fig. 2A) are consistent with a complete topological rearrangement of liposomes and DNA into a multilayer structure with DNA intercalated between the bilayers (*24*) (Fig. 3A). Two sharp peaks at q = 0.0965 ± 0.003 and 0.193 ± 0.006 $Å^{-1}$ correspond to the (001) peaks of a layered structure with an interlayer spacing d (= $\delta_m + \delta_w$), which is in the range 65.1 ± 2 Å (Fig. 2B, open squares).

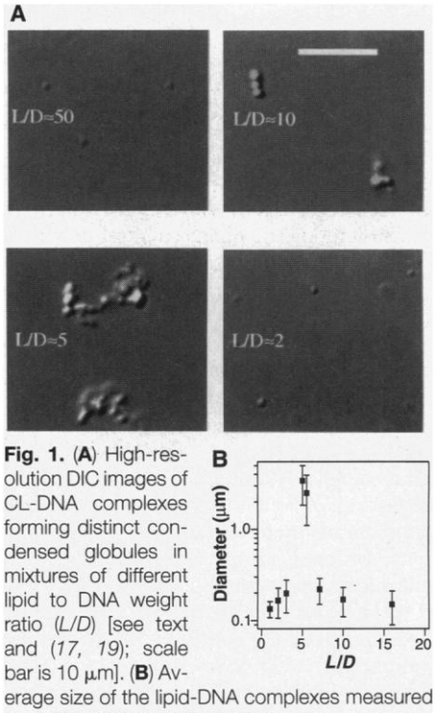

Fig. 1. (**A**) High-resolution DIC images of CL-DNA complexes forming distinct condensed globules in mixtures of different lipid to DNA weight ratio (*L*/*D*) [see text and (*17*, *19*); scale bar is 10 μm]. (**B**) Average size of the lipid-DNA complexes measured by dynamic light scattering (*18*).

The membrane thickness and water gap are denoted by δ_m and δ_w, respectively (Fig. 3A). The middle broad peak q_{DNA} arises from DNA-DNA correlations and gives $d_{DNA} = 2\pi/q_{DNA}$ (Fig. 2B, solid circles). The multilamellar structure with intercalated DNA is also observed in CL-DNA complexes containing supercoiled DNA both in water and in Dulbecco's modified Eagle's medium used in transfection experiments in gene therapy applications (*25*). This novel multilamellar structure of the CL-DNA complexes protected DNA from being cut by restriction enzymes (*26*).

In the absence of DNA, membranes comprised of mixtures of DOPC and the cationic lipid DOTAP (1:1) exhibited strong long-range interlayer electrostatic repulsions that overwhelm the van der Waals attraction (*27, 28*). In this case, as the volume fraction Φ_w of water was increased, the L_α phase swelled and d could be obtained from the simple geometric relation $d = \delta_m/(1 - \Phi_w)$ (*27*). The SAXS scans in Fig. 2C show this behavior with the (001) peaks moving to lower q as Φ_w increases. From d ($= 2\pi/q_{(001)}$) at a given Φ_w, we obtain $\delta_m = 39 \pm 0.5$ Å for DOPC/DOTAP (1:1). Liposomes made of DOPC/DOTAP (1:1) with $\Phi_w \approx 98.5\%$ did not exhibit Bragg diffraction in the small wave vector range covered in Fig. 2A.

The DNA that condenses on the CLs strongly screens the electrostatic interaction between lipid bilayers and leads to condensed multilayers. The average thickness of the water gap $\delta_w = d - \delta_m = 65.1$ Å − 39 Å = 26.1 ± 2.5 Å is just sufficient to accommodate one monolayer of B-DNA (diameter ≈ 20 Å) including a hydration shell (*29*). We see in Fig. 2B that d is almost constant, as expected for a monolayer DNA intercalate (Fig. 3A). In contrast, as L/D decreased from 18 to 2, d_{DNA} suddenly decreased from ~44 Å in the positively charged regime just above $L/D = 5$ (near the stoichiometric charge neutral point) to ~37 Å for the negatively charged regime (Fig. 2B). In these distinct regimes, lamellar condensates coexist with excess giant liposomes in the positive regime and with excess DNA in the negative regime (*30*).

The driving force for higher order self-assembly is the release of counterions. DNA carries 20 phosphate groups per helical pitch of 34.1 Å, and due to Manning condensation 76% of these anionic groups are permanently neutralized by their counterions, which leads to a distance between anionic groups ≈ the Bjerrum length = 7.1 Å (*31*). During condensation, the cationic lipid tends to fully neutralize the phosphate groups on the DNA, in effect replacing and releasing the originally condensed counterions (both those bound to the 1D DNA and to the 2D cationic membranes) in solution.

To improve on the signal-to-background intensity ratio, the synchrotron XRD experiments were carried out at concentrations (lipid + DNA ≈ 1.4 ± 0.3% volume in water), which, although dilute (*24*), were nevertheless greater than the concentrations used in the microscopy work (*17, 19*). A typical SAXS scan in mixtures at the optical microscopy concentrations (Fig. 1A) is shown in Fig. 2A (inset), which exhibits the same features and confirms that the local multilayer and DNA structure (Fig. 3A) is unchanged between the two concentrations. The x-ray samples consisted of connected yet distinct globules (Fig. 3B). What is remarkable is the retention of the globule morphology consistent with what was observed at lower concentrations in DIC (Fig. 1A). Under crossed polarizers (Fig. 3C), LC defects, both focal conics and spherulitic defects (*32*), resulting from the smectic-A–like layered structure of the DNA-lipid globules, are evident. The globules at the lower concentrations (Fig. 1A) show similar LC defects.

We further probed the nature of λ-DNA packing within the lipid layers by conducting a lipid dilution experiment in the isoelectric point regime of the complex. The total lipid (L = DOTAP + DOPC) was increased while the charge of the overall complex, given by the ratio of cationic DOTAP to DNA, was kept constant at DOTAP/DNA = 2.45 ± 0.15 (*33*). The SAXS scans in Fig. 4A (arrow points to the DNA peak) show that $d_{DNA} = 2\pi/q_{DNA}$ increased, with lipid dilution from 24.54 to 57.1 Å as L/D increased with lipid dilution between 2.45 and ≈9 (Fig. 4B). The most compressed interaxial spacing of 24.55 Å at $L/D = 2.45$ approaches the short-range, repulsive hard-core interaction of the B-DNA rods containing a hydration layer (*29*).

The DNA interaxial spacing can be calculated rigorously from simple geometric considerations. If we assume that all of the DNA is adsorbed between the bilayers and that the orientationally ordered DNA chains separate to fill the increasing lipid area as L/D increases, while maintaining a 1D lattice (Fig. 3A), then

$$d_{DNA} = \frac{A_D \rho_D}{\delta_m \rho_L} (L/D) \qquad (1)$$

Here, $\rho_D = 1.7$ (g/cc) and $\rho_L = 1.07$ (g/cc) denote the densities of DNA and lipid, respectively; δ_m the membrane thickness; and A_D the DNA area [$A_D = Wt(\lambda)/(\rho_D L(\lambda)) = 186$ Å^2, $Wt(\lambda)$ = weight of λ-DNA = $31.5 \times 10^6/(6.022 \times 10^{23})$ g and $L(\lambda)$ = contour length of λ-DNA = 48502×3.4 Å]. The solid line in Fig. 4B is then obtained from Eq. 1 with no adjustable parameters and shows a remarkable agreement with the data over the measured interaxial distance from 24.5 to 57.1 Å. The observed deviation from linear behavior both in the data and the solid line arises from the slight increase in δ_m as L/D increases (*34*). The existence of a finite-sized

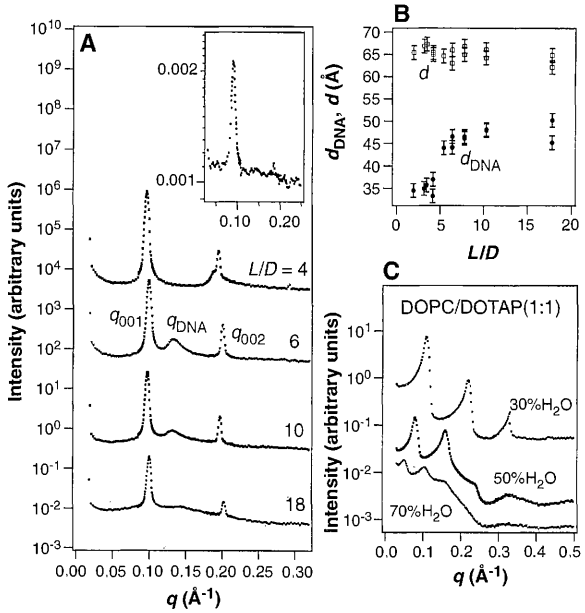

Fig. 2. (**A**) A series of SAXS scans of CL-DNA complexes in excess water as a function of different lipid to DNA weight ratio (L/D). The Bragg reflections at $q_{001} = 0.096$ Å^{-1} and $q_{002} = 0.1.92$ Å^{-1} result from the multilamellar L_α structure with intercalated monolayer DNA (see Fig. 3A). The intermediate peak at q_{DNA} is due to the DNA-interaxial spacing d_{DNA} as described in the text. (Inset) SAXS scan of an extremely dilute (lipid + DNA = 0.014% volume in water) λ-DNA–DOPE/DOTAP (1:1) complex at $L/D = 10$, which shows the same features as the more concentrated mixtures and confirms the multilamellar structure (with alternating lipid bilayer and DNA monolayers) of very dilute mixtures typically used in gene therapy applications. (**B**) The spacings $d = \delta_m + \delta_w$ and d_{DNA} (see Fig. 3A for notation) as a function of L/D show that (i) d is nearly constant and (ii) two distinct regimes of DNA packing, one where the complexes are positive ($L/D > 5$, $d_{DNA} \approx 46$ Å) and the other regime where the complexes are negative ($L/D < 5$, $d_{DNA} \approx 35$ Å). (**C**) SAXS scans of the lamellar L_α phase of DOPC/DOTAP (cationic)–water mixtures done at lower resolution (rotating-anode x-ray generator). A dilution series of 30% (d = 57.61 Å), 50% (d = 79.49 Å), and 70% (d = 123.13 Å) H_2O by weight is shown.

ordered lattice is made unambiguous from the linewidths of the DNA peaks (Fig. 4A), where we find that the 1D lattice of DNA chains has a correlated domain size extending to near 10 unit cells (Fig. 4C). Thus, the DNA chains form a 1D ordered array adsorbed between 2D membranes; that is, they form a novel finite-sized 2D smectic phase. Beyond $L/D > 10$ we found multiphase behavior (*35*).

The lattice expansion at the isoelectric point covering interaxial distances with negligible short-range hydration forces (*29*) (B-DNA diameter ≈ 20 Å) is indicative of a long-range repulsion. The distribution of the counterion lipid (DOTAP) concentration according to the Poisson-Boltzmann equation along the top and bottom monolayer that bound the DNA molecules (Fig. 3A) will lead to a long-range electrostatic-induced interhelical interaction from the counterion lipid pressure (due to the expected local demixing of the cationic and neutral lipids) and the electric field. Preliminary salt-dependent experiments (*35*), which show shifts in the DNA peak, indicate that long-range electrostatic-induced interactions are present. Additionally, because of the semiflexible nature of λ-DNA [consisting of between 170 and 340 persistence lengths (ξ_p) in dilute solution ($\xi_p \approx$ between 500 and 1000 Å)], we expect the long-range repulsions to be further enhanced by chain-undulation interactions. A similar enhancement has been observed in a hexagonal lattice of DNA (*29*, *36*). This phase of 1D DNA chains is the lower dimensional analog of 2D fluid membranes in that it may either be dominated by electrostatic-induced forces (*27*, *28*) or the interplay between electrostatics and undulations (*37*–*39*).

Further experiments are needed to elucidate the precise nature of the intermolecular forces and the interplay between electrostatic and chain undulation interactions (*40*). Future studies may also reveal regimes with 3D correlations between the DNA chains from layer to layer in analogy to

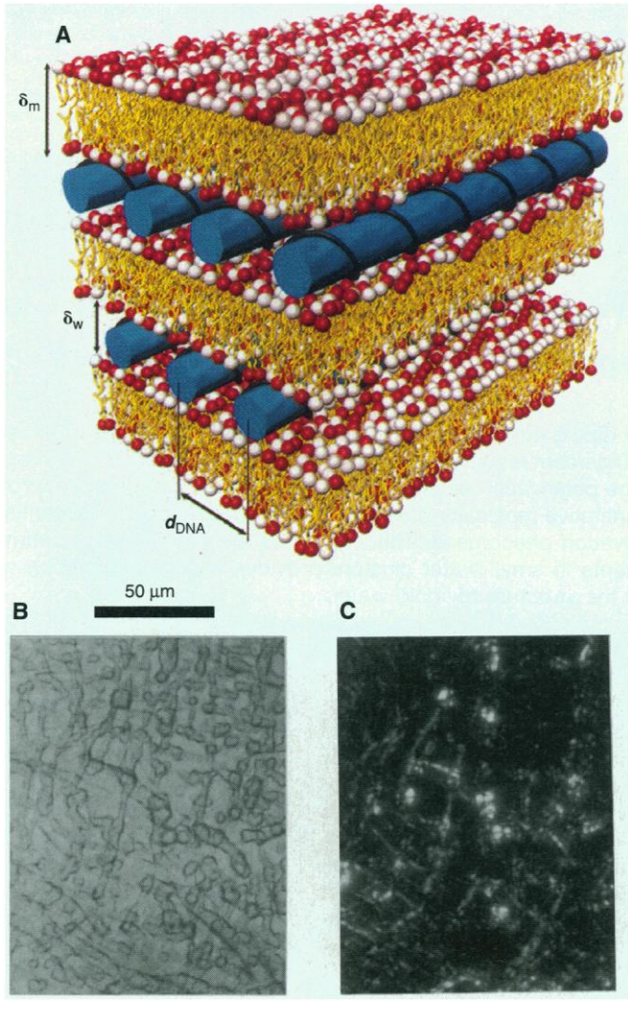

Fig. 3. (**A**) Schematic picture of the local arrangement in the interior of lipid-DNA complexes (shown at two different concentrations in Fig. 1A and in (**B**) below. The semiflexible DNA molecules are represented by rods on this molecular scale. The neutral and cationic lipids comprising the membrane are expected to locally demix with the cationic lipids (red) more concentrated near the DNA. Micrographs of DNA-lipid condensates under (B) bright light and (**C**) crossed polarizers showing LC-like defects.

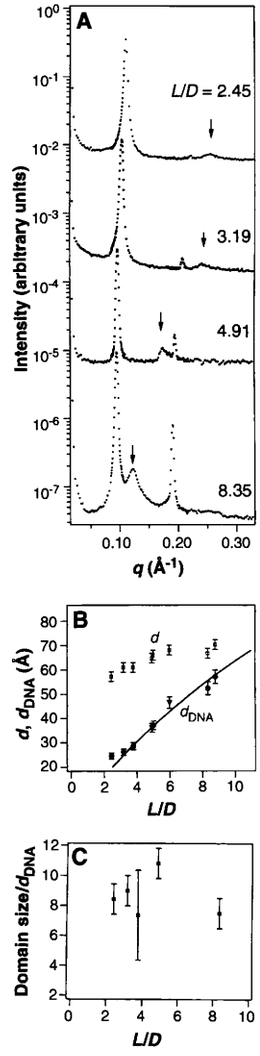

Fig. 4. (**A**) A series of SAXS scans of CL-DNA complexes at DOTAP/DNA = 2.4 ± 0.1 (approximately the isoelectric point) which shows the DNA peak (arrow) moving toward smaller q as L/D increases (that is, increasing the DOPC to DOTAP ratio at a constant DOTAP/DNA; L = DOTAP + DOPC, D = DNA). (**B**) d_{DNA} and $d = \delta_m + \delta_w$ from (A) plotted as a function of L/D (see Fig. 3A for notation). Circles are synchrotron data, and triangles are rotating anode. The solid line is the prediction of a packing calculation (with no adjustable parameters) where the DNA chains form a space-filling 1D lattice. (**C**) The average domain size of the 1D lattice of DNA chains derived from the width of the DNA peaks shown in (A) [corrected for resolution and powder averaging broadening effects; for example, see (*27*, *38*)].

recent theoretical findings in highly condensed DNA phases (*41*). The observed quantitative control over the structural nature of the DNA packing in CL-DNA complexes may lead to a better understanding of the important structural parameters relevant to transfection efficiencies in gene therapy (*26*); in particular, they should be directly relevant to our understanding of the interactions of the complex with cellular lipids and the mechanism of DNA transfer across the nuclear membrane.

REFERENCES AND NOTES

1. R. G. Crystal, *Science* **270**, 404 (1995); R. C. Mulligan, *ibid.* **260**, 926 (1993).
2. P. L. Felgner and G. Rhodes, *Nature* **349**, 351 (1991); J.-P. Behr, *Bioconjug. Chem.* **5**, 382 (1994); A. Singhal and L. Huang, *Gene Therapeutics: Methods and Applications of Direct Gene Transfer*, J. A. Wolff, Ed. (Birkhauser, Boston, 1994).
3. P. L. Felgner *et al.*, *Proc. Natl. Acad. Sci. U.S.A.* **84**, 7413 (1987).
4. N. Zhu, D. Liggitt, Y. Liu, R. Debs, *Science* **261**, 209 (1993).
5. G. J. Nabel *et al.*, *Proc. Natl. Acad. Sci. U.S.A.* **90**, 11307 (1993); N. M. Caplen *et al.*, *Nature Med.* **1**, 39 (1995).
6. D. Lasic and N. S. Templeton, *Adv. Drug Deliv. Rev.*, in press.
7. E. Marshall, *Science* **269**, 1050 (1995); *ibid.* **270**, 1751 (1995).
8. V. A. Bloomfield, *Biopolymers* **31**, 1471 (1991).
9. F. Livolant, A. M. Levelut, J. Doucet, J. P. Benoit, *Nature* **339**, 724 (1989).
10. Z. Reich, E. J. Wachtel, A. Minsky, *Science* **264**, 1460 (1994).
11. E. Sackmann, *ibid.* **271**, 43 (1996); C. Ligoure, G. Bouglet, G. Porte, *Phys. Rev. Lett.* **71**, 3600 (1993).
12. H. E. Warriner, S. H. J. Idziak, N. L. Slack, P. Davidson, C. R. Safinya, *Science* **271**, 969 (1996); A. K. Kemworthy, K. Hristova, D. Needham, T. J. McIntosh, *Biophys. J.* **68**, 1921 (1995).
13. H. Gershon, R. Ghirlando, S. B. Guttmann, A. Minsky, *Biochemistry* **32**, 7143 (1993).
14. J. Gustafsson, G. Arvidson, G. Karlsson, M. Almgren, *Biochim. Biophys. Acta* **1235**, 305 (1995).
15. B. Sternberg, F. L. Sorgi, L. Huang, *FEBS Lett.* **356**, 361 (1994).
16. S. B. Smith, L. Finzi, C. Bustamante, *Science* **258**, 1122 (1992); T. T. Perkins, D. E. Smith, S. Chu, *ibid.* **264**, 819 (1994).
17. A mixture of DOPE/DOTAP (1:1, wt:wt) was prepared in a 20-mg/ml chloroform stock solution; 500 ml was dried under nitrogen in a narrow glass beaker and desiccated under vacuum for 6 hours. After addition of 2.5 ml of Millipore water and 2 hours incubation at 40°C, the vesicle suspension was sonicated to clarity for 10 min. The resulting solution of liposomes (25 mg/ml) was filtered through 0.2-μm Nucleopore filters. For optical measurements, the concentration of SUV used was between 0.1 and 0.5 mg/ml. All the lipids were purchased from Avanti Polar Lipids, Inc. (Alabaster, AL).
18. The liposome and complex sizes were measured by dynamic light scattering (Microtrac UPA 150, Leeds and Northrup).
19. Purified λ-phage DNA and pBR322 plasmid were purchased from Biolabs, New England. Optical and x-ray data were taken with linear λ prepared in two ways: (i) used as delivered, and (ii) by heating to 65°C and reacting with a surplus of a 12-base oligo complementary to the 3′ COS end. Subsequently, the DNA was ligated (T4 DNA ligase, Fischer). The methods gave the same result. For the optical experiments, the DNA concentration used was between 0.01 and 0.1 mg/ml.
20. A. Nikon Diaphot 300 equipped for epifluorescence and high-resolution DIC was used.
21. Sonicated DOPE-DOTAP (1:1) liposomes were prepared at 0.1 mg/ml with 0.2 mol % DHPE–Texas Red fluorescence label. DNA stained by YOYO (Molecular Probes) was added under gentle mixing at different *L/D*s.
22. J. O. Rädler, I. Koltover, T. Salditt, A. Jamieson, C. R. Safinya, unpublished results.
23. High-resolution synchrotron x-ray scattering was performed at the Stanford Synchrotron Radiation Laboratory. Lower resolution XRD experiments were performed with a rotating anode source.
24. The DNA-lipid condensates were prepared from a 25-mg/ml liposome suspension and a 5-mg/ml DNA solution. The solutions were filled in 2-mm–diameter quartz capillaries with different ratios *L/D*, respectively, and mixed after flame sealing by gentle centrifugation up and down the capillary.
25. A. Lin, N. Slack, S. H. J. Idziak, C. R. Safinya, unpublished results.
26. The intercalation of λ-DNA between membranes in CL-DNA complexes was found to protect it against a Hind III restriction enzyme, which cuts naked λ-DNA at seven sites (*22*).
27. D. Roux and C. R. Safinya, *J. Phys. (France)* **49**, 307 (1988).
28. C. R. Safinya, in *Phase Transitions in Soft Condensed Matter*, R. Tormod and D. Sherrington, Eds. (Plenum, New York, 1989), pp. 249–270.
29. R. Podgornik, D. C. Rau, V. A. Parsegian, *Macromolecules* **22**, 1780 (1989).
30. The multilamellar structure of the complex (with λ-DNA) and the distinct DNA interhelical packing regimes were also found in SAXS data in binary mixtures of cationic lipids that contained DOPE [which has a high transfection efficiency (*2*)] as the neutral colipid. However, the complexes showed a phase separation into two condensed phases.
31. G. S. Manning, *J. Chem. Phys.* **51**, 924 (1969).
32. P. Boltenhagen, O. D. Lavrentotovich, M. Kleman, *Phys. Rev. A* **46**, 1743 (1992).
33. The projected charge density of DNA (two anionic charges per 68 Å^2) is nearly matched by two cationic head groups on DOTAP of ~70 Å^2 each and thus permits near complete neutralization of the complex (Fig. 3A).
34. The variation in the interlayer spacing d ($= \delta_w + \delta_m$) (Fig. 4B) arises from the increase in the membrane bilayer thickness δ_m as *L/D* increases (each DOPC molecule is ~4 to 6 Å longer than a DOTAP molecule). δ_m was obtained at each *L/D* by measuring d in the L_α phase multilayer membranes at the corresponding DOTAP to DOPC ratio and using the relation $\delta_m = d(1 - \Phi_w)$, Φ_w = water volume fraction. The measured δ_m and d, gave $\delta_w = 25 \pm 1.5$ Å, close to the spacing for the DNA monolayer (see Fig. 3A).
35. I. Kolover, T. Salditt, J. Rädler, C. R. Safinya, unpublished results.
36. J. V. Selinger and R. F. Bruinsma, *Phys. Rev. A* **43**, 2922 (1991).
37. W. Helfrich, *Z. Naturforsch. Teil A* **33**, 305 (1978).
38. C. R. Safinya *et al.*, *Phys. Rev. Lett.* **57**, 2718 (1986).
39. E. A. Evans and V. A. Parsegian, *Proc. Natl. Acad. Sci. U.S.A.* **83**, 7132 (1986).
40. N. Dan, *Biophys. J.*, in press.
41. R. D. Kamien and D. R. Nelson, *Phys. Rev. E* **53**, 650 (1996).

42. We acknowledge useful discussions with R. Bruinsma, N. Dan, W. Gelbart, P. Pincus, J. Prost, T. Lubensky, and D. Lasic. Supported in part by NSF grant DMR-9624091, the Petroleum Research Fund (31352-AC7), and a Los Alamos CULAR grant STB/UC:96-108. J.O.R. and T.S. acknowledge partial support by DFG (Ra 655/1-1) and DAAD scholarships, respectively. The Materials Research Laboratory at Santa Barbara is supported by the NSF under grant DMR-9632716. The synchrotron experiments were carried out at Stanford (SSRL) supported by the U.S. Department of Energy.

17 July 1996; accepted 24 October 1996

The Water Dipole Moment in Water Clusters

J. K. Gregory, D. C. Clary,* K. Liu, M. G. Brown, R. J. Saykally

The average dipole moment of a water molecule in the condensed phase is enhanced by around 40 percent relative to that of an isolated monomer. This enhancement results from the large polarization caused by the electric field induced by surrounding monomers. A quantitative molecular description of this polarization is essential for modeling aqueous solvation phenomena. This combined theoretical and experimental study of dipole moments in small water clusters provides such a description and also gives insights into the structure of liquid water.

Water clusters have been studied extensively both experimentally (*1*) and theoretically (*2–4*) in recent years. Their study provides a means of systematically explaining the properties of the bulk liquid, which exists as an extended and dynamic hydrogen-bonded network (*5*). The research area has witnessed rapid advances as a result of new experimental and computational techniques (*6*). The ultimate goals are the development of an accurate many-body potential energy surface (PES) that describes the electronic energy of a system of interacting water molecules and of a quantitative description of the condensed phases of water (*7*).

The dipole moment of an isolated water monomer is 1.855 D (*8*), whereas the corresponding value in the condensed phase increases from 2.4 to 2.6 D as a result of polarization by the environment (*9*) (the debye unit D = 3.336×10^{-30} C/m). Theoretical treatments based on ice lattices have suggested even higher values of about 3.0 D (*10*). Simulations of condensed water based on the use of pairwise additive potentials generally require exaggerated mono-

J. K. Gregory, Department of Chemistry, University of Cambridge, Cambridge CB2 1EW, UK.
D. C. Clary, Department of Chemistry, University College London, London WC1H OAJ, UK.
K. Liu, M. G. Brown, R. J. Saykally, Department of Chemistry, University of California, Berkeley, CA 94720, USA.

*To whom correspondence should be addressed.